SCIEPublish

Article

Dynamic Oxidation Behavior and Exceptional High-Temperature Resistance of Nano Particle-Strengthened Superalloy (MA 754) under Cyclic Temperature Conditions

Afsaneh Moosaei and Mohammad Jafar Hadianfard *

Department of Materials Science and Engineering, School of Engineering, Shiraz University, Shiraz 7134851154, Iran; afsaneh.musaie@gmail.com (A.M.)

* Corresponding author. E-mail: hadianfa@shirazu.ac.ir (M.J.H.)

Received: 3 April 2025; Accepted: 20 June 2025; Available online: 27 June 2025

ABSTRACT: The degradation of industrial components due to high-temperature oxidation poses a significant challenge. This study highlights the excellent oxidation resistance of the MA 754 superalloy under cyclic high-temperature conditions at 1100 °C. The weight change during thermal cycles was measured to assess the kinetics of oxidation. Optical microscopy, scanning electron microscopy, X-ray diffraction, and energy dispersive spectroscopy were used to characterize the oxide scales' microstructure, morphology, phases, and composition. The results revealed that the MA 754 superalloy demonstrated excellent resistance to oxidation, with a mean net mass change of 0.032 mg/cm^2 over the oxidation time. The oxidation products identified were NiO and $NiCr_2O_4$. A small peak suggests the possible formation of Al_2O_3. The oxide scales' morphology changed from pyramidal to granular type during the oxidation test. The oxidation steps of the MA 754 superalloy were determined by comparing the microstructures of the alloy surface next to the oxide layer.

Keywords: Cyclic oxidation; Nickel-based superalloy; MA 754; Oxide pyramids

1. Introduction

The degradation of high-temperature components is mainly attributed to loss of strength and oxidation at elevated temperatures [1–3]. It is well known that exposure to high temperatures significantly decreases the lifespan of materials due to oxidation. Therefore, different classes of alloys are utilized depending on the temperature requirements [4]. Ni-based superalloys are a suitable choice for high-temperature applications due to their ability to resist corrosion and oxidation by forming protective oxides in an oxidizing environment [2,4–9]. An important class of Ni-based superalloys, known as oxide dispersion-strengthened (ODS) alloys, has been developed by incorporating nanoparticles into the matrix alloy, which helps to control the loss of strength and improve creep resistance [10–12]. The MA 754 alloy is one of the first ODS alloys, and it is strengthened by the dispersion of nano yttrium oxide particles within a corrosion-resistant matrix [10–12].

Numerous investigations have explored the oxidation behavior of various classes of Ni-based superalloys [8,13–16]. Quadakkers [17] reported that oxide dispersion-strengthened (ODS) alloys exhibit superior oxidation resistance compared to non-ODS alloys. It has been recognized that the oxidation resistance of the MA 754 superalloy is attributed to forming a protective Cr_2O_3 oxide layer. In a study by Mutoh et al. [18], several Ni-based superalloys, including MA 754, were subjected to corrosion investigation in an impure helium gas environment at 1373 K under simulated conditions of nuclear reactors. The results of their study indicated that MA 754 exhibits high resistance against oxidative environments. Natesan et al. [19] reported that the low oxidation rate of MA 754 is due to the presence of Al, Cr, and Y_2O_3 particles.

Given the excellent resistance of Ni-based superalloys such as MA 754 to oxidation at high temperatures, it is valuable to investigate their oxidation behavior and properties under such conditions. Although the oxidation resistance of the MA 754 superalloy has been investigated in previous studies, most existing work has focused on isothermal

https://doi.org/10.70322/amsm.2025.10009

oxidation or has been conducted under different atmospheric conditions. In practical applications, however, components are often subjected to cyclic thermal loading due to start-up and shutdown operations, which induce thermal stresses in the oxide scale and significantly influence oxidation behavior. Therefore, this study focuses on the cyclic oxidation performance of MA 754 at 1100 °C in air containing 6% moisture, as these conditions more accurately reflect real service environments. In addition to evaluating oxidation kinetics, this work provides detailed insights into oxide scale morphology, phase evolution, and stress-driven spallation mechanisms—areas that remain insufficiently explored in the existing literature.

2. Experimental Procedures

The alloy used during this study is Ni-based superalloy, which is near to the composition of the MA 754. The chemical composition of the alloy is shown in Table 1.

Table 1. The chemical composition of the studied alloy (wt. %).

Alloy	Ni	Cr	Al	Ti	Fe	C	Y_2O_3
MA 754	Bal.	20	0.5	0.3	1	0.05	0.6

The Ni-based superalloy's high-temperature cyclic oxidation behavior was evaluated using the mass change measurement technique. In this technique, samples with a known surface area are exposed to an oxidizing atmosphere in a furnace, and the mean net mass change of the samples is determined at specific intervals of oxidation time. The selection of heating and cooling intervals and oxidation temperature is proportional to the operational condition of the alloy. The high-temperature cyclic oxidation study was conducted according to the ISO 13573 standard for 100 h. Each cycle consisted of 1 h of heating at 1100 °C, followed by 15 min of cooling at room temperature. The mass change was measured every two thermal cycles to determine the oxidation kinetics.

Cylindrical specimens, measuring 5 mm in diameter and 2 mm in height, were obtained from the hot extruded wire to conduct the cyclic oxidation test. To ensure the reliability of the measurements, three test pieces were utilized. First, the samples were ground with 200, 400, 600, and 1000 SiC abrasive papers, and their weight was measured with a digital balance with a precision of 0.1 mg before being subjected to the oxidation environment. Next, the samples were degreased using acetone. For the oxidation tests, three alumina boats were used, and volatile compounds were removed by baking the boats for 24 h at a temperature of 1000 °C. The specimens were then placed in the boats and dried at 100 °C for 30 min before being inserted into a muffle furnace for the cyclic oxidation test. After removing the specimens from the furnace, loosely adherent oxide scales were gently removed by tapping the test samples inside the boats to collect the spalled scale. The mass change was determined by making three measurements for each test piece. Finally, the mean net mass change of the three test samples was plotted versus time.

The oxidation products were characterized by energy-dispersive spectroscopy (EDS) and X-ray diffraction (XRD). The microstructure and morphology of oxidized samples have been investigated by optical and scanning electron microscopes. For microstructural characterization, samples were etched in 10 g $CuSO_4$ + 50 mL HCl + 50 mL water solution for 20 s.

3. Results and Discussion

3.1. Cyclic Oxidation Behavior

The mean net mass change of samples after cyclic oxidation test in air containing 6% moisture at 1100 °C versus exposure time is presented in Figure 1.

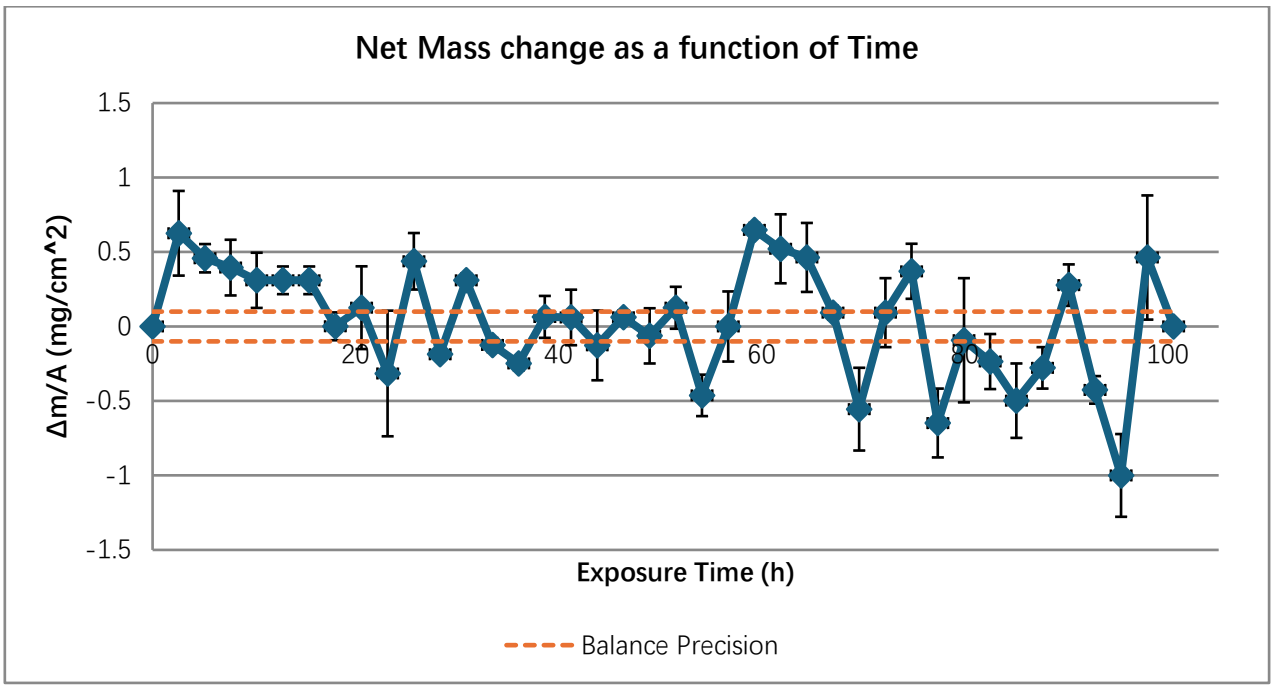

Figure 1. Mean net mass change of the MA 754 superalloy oxidized in air at 1100 °C, as a function of exposure time.

The increase in the weight of the samples is associated with the reaction between the superalloy and oxygen in the surrounding air, resulting in the formation of oxide scales. Conversely, the weight loss of the samples can be attributed to the cracking of the protective oxide film, leading to its spallation from the surface of the superalloy. These cracking and spallation phenomena are the consequences of thermal and oxide growth stresses. The observed fluctuations in the oxidation behavior may be partially attributed to experimental apparatus errors. Similar oxidation behavior was documented by Obigodi-Ndjeng [4] during the investigation of the oxidation behavior of Ni-based superalloy PWA and Ni-Cr-Al ternary alloys. The author concluded that a fluctuating curve might indicate a non-steady oxidation behavior.

3.2. Oxidation Products

Figure 2 presents the XRD spectra depicting the spalled oxides of MA 754 superalloy following 100 h of cyclic oxidation at a temperature of 1100 °C. The obtained results reveal that the oxidation products of this Inconel alloy primarily consist of NiO and $NiCr_2O_4$. A small peak at approximately 25.6° in the XRD pattern, which does not overlap with other phases, suggests the possible presence of α-Al_2O_3. Notably, the prominent peaks corresponding to NiO suggest that this oxide constitutes the predominant component of the oxide scale during the cyclic oxidation process of MA 754, whereas Al_2O_3 exhibits the least formation. Considering that MA 754 superalloy is known as a chromia-forming alloy when exposed to an oxidizing atmosphere [13], the presence of Cr_2O_3 peaks in the XRD pattern is expected. However, the absence of Cr_2O_3 in the oxidation products can be attributed to the following two reasons:

Previous investigations have indicated that the protective chromium oxide scale reacts with O_2 at elevated temperatures following reaction 1, forming gaseous CrO_3.

$$Cr_2O_3 + 3/2\ O_2 \rightarrow 2\ CrO_3 \quad (1)$$

The Gibbs free energy (ΔG) for this reaction at 1100 °C is calculated to be approximately +240 kJ·mol^{-1}. This positive value suggests that CrO_3 formation is not spontaneous under standard conditions. However, the process is promoted by high oxygen partial pressure and the presence of water vapor, which was 6% in the test environment. These conditions facilitate chromium volatilization through the formation of CrO_3 and volatile chromium oxyhydroxide species such as $CrO_2(OH)_2$, thereby contributing to the observed depletion of Cr_2O_3 from the scale [20–24].

Simultaneously, the protective chromium oxide reacts with NiO during high-temperature oxidation, forming non-protective $NiCr_2O_4$ [5,15]. This reaction can be represented by reaction 2 [5]:

$$NiO + Cr_2O_3 \rightarrow NiCr_2O_4 \quad (2)$$

The Gibbs free energy equation associated with this reaction is given by:

$$\Delta G\ (T) = -137.26 + 0.3677T\ (kJ \cdot mol^{-1}) \quad (3)$$

Consequently, the value of ΔG (T) for $NiCr_2O_4$ at 1100 °C is approximately −873.31 $kJ \cdot mol^{-1}$. The negative value of ΔG (T) confirms the thermodynamic favorability of $NiCr_2O_4$ formation. Therefore, from a thermodynamic standpoint, the spontaneous formation of this spinel from its reactants is established.

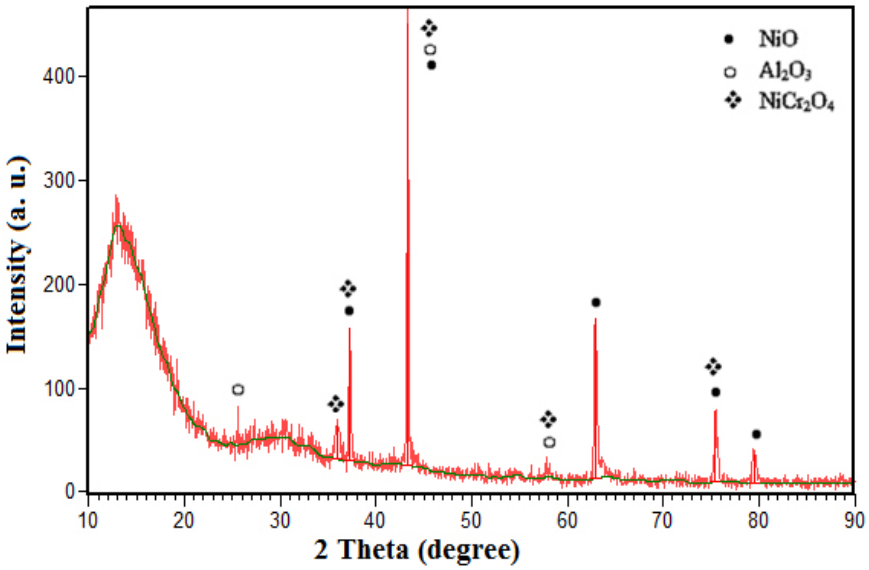

Figure 2. XRD pattern of the spalled oxides of MA 754 superalloy after 100 h cyclic oxidation in air at 1100 °C.

One approach to forecasting the formation of oxides during an alloy's oxidation involves using an oxide map. Figure 3 depicts the oxide map corresponding to a ternary Ni-Cr-Al system at a temperature of 1100 °C. This diagram encompasses three distinct regions. The position of MA 754 within this superalloy is determined by the atomic percentages of Ni, Cr, and Al in its chemical composition. The star symbol in Figure 3 indicates the determined location of the alloy under investigation, situated next to the NiO/Cr_2O_3 boundary of the ternary diagram within the NiO region. According to Khanna [2], oxides formed in alloys belonging to this region predominantly consist of NiO and spinels, with the possibility of internal oxidation of Cr and Ni. Within this region, the oxidation process is primarily governed by the outward diffusion of Ni ions. Hence, the presence of NiO and $NiCr_2O_4$, along with the absence of Cr_2O_3, in the XRD pattern of the spalled oxide (Figure 2) can be predicted using the oxide map.

However, the small Al_2O_3 peak observed in the XRD pattern (Figure 2), despite the alloy composition placing it in the NiO region of the oxide map (Figure 3), suggests the occurrence of localized or internal oxidation processes. This can be attributed to several factors. First, aluminum, though present in low bulk content (0.5 wt.%), may locally concentrate near grain boundaries or oxide dispersion particles such as Y_2O_3, enabling the nucleation of Al_2O_3 [2,17,25]. Second, aluminum's strong affinity for oxygen allows for internal oxidation below the surface, leading to subscale Al_2O_3 formation that may only be revealed through spallation or cracking of the outer layers [26,27]. Third, cyclic oxidation in moist air (6% water vapor) can modify oxidation kinetics and favor the transient formation of Al_2O_3 even in low-Al alloys [23,24]. Thus, although not predicted as a major oxide by the equilibrium oxide map, the minor presence of Al_2O_3 is thermokinetically plausible under the current experimental conditions.

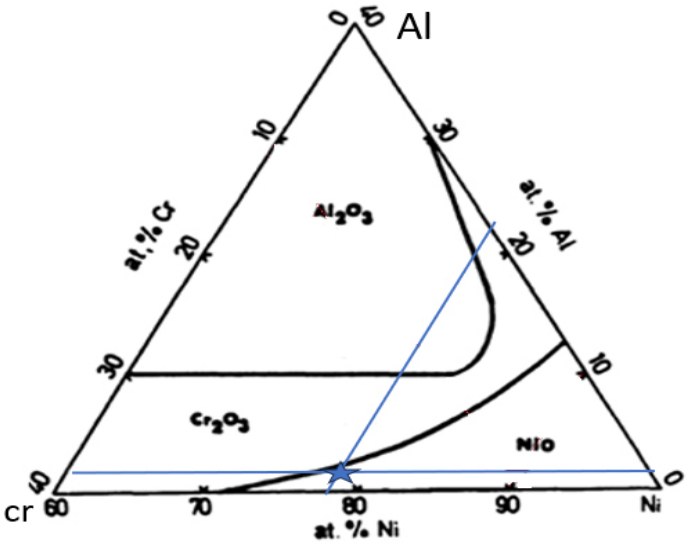

Figure 3. Oxide map for alloys in the ternary Ni-Cr-Al system at 1100 °C [28].

3.3. Scale Morphology and Elemental Composition

The surface morphology of the MA 754 sample was analyzed using scanning electron microscopy (SEM), as illustrated in Figure 4. The observed image reveals a porous and extensively cracked oxidized surface. The occurrence of cracks serves as an indication of stress concentration within the oxide scale [2]. Based on the findings depicted in Figure 4a, it can be inferred that the MA 754 samples underwent oxide spallation phenomena during the high-temperature oxidation test. Consequently, this particular superalloy mitigates stress concentration by forming cracks in the scale, thereby facilitating scale spallation. A primary factor contributing to oxide spallation is thermal stress, arising from a mismatch between the thermal expansion coefficients of the oxide and the alloy [2]. Given that the oxidation test was conducted under cyclic temperature conditions, the samples experienced repeated cooling and heating cycles. As a result, the cyclic heating conditions not only generated stress within the oxide layer but also led to the accumulation of thermal stresses, thereby promoting scale spallation during the oxidation study [2].

An additional factor contributing to oxide spallation is the generation of stress during the growth of oxide scales [2]. Non-protective oxides, such as NiO and $NiCr_2O_4$, exhibit a higher growth rate compared to protective oxides like Al_2O_3 [29]. Considering the XRD pattern (Figure 2), which indicates that NiO and $NiCr_2O_4$ are the primary constituents of the oxidation products of MA 754, it can be inferred that the studied alloy experienced elevated stresses during the growth of oxides. These stresses progressively accumulate during the oxidation of the alloy, ultimately leading to the spallation of the oxide layers.

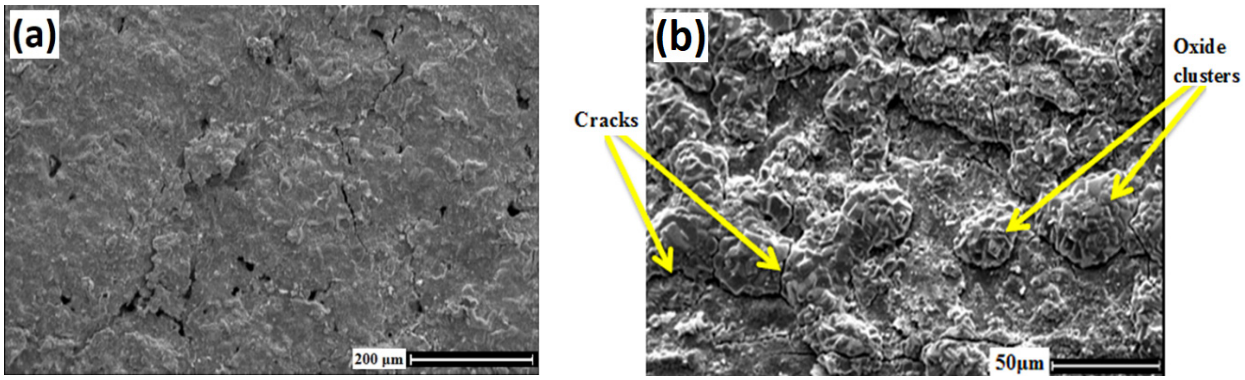

Figure 4. SEM surface morphology of the MA 754 sample after 50 h cyclic oxidation at 1100 °C: (**a**) Lower magnification showing overall cracked and porous oxide layer, (**b**) Higher magnification highlighting flower-like oxide clusters (yellow arrows).

Figure 4b presents a higher magnification of the same region, revealing the detailed flower-like oxide clusters (indicated by yellow arrows). It can be observed that each distinct oxide cluster has a flower-like structure.

To provide a more comprehensive understanding of the morphology of oxide clusters, higher-magnification images are presented in Figure 5. These images depict the morphology of spalled oxides and the oxidized sample after a 50 h

cyclic oxidation test at 1100 °C. The SEM micrographs reveal a pyramidal-type morphology characterized by flat faces. Notably, each oxide cluster exhibits a flower-like structure composed of numerous oxide pyramids. In addition, the pyramidal oxides observed in Figure 5 are remarkably small, with approximate dimensions below 6 µm.

Raynaud et al. [30] and Tawancy [31] previously observed the pyramidal-type morphology of oxides during the oxidation behavior of Ni alloys. In this particular mode of oxide growth, screw dislocations facilitate the creation of new steps, and the growth process occurs through either lattice or grain boundary diffusion [30]. The formation of pyramid-shaped oxides is driven by the depreciation of the system's surface energy, thereby influencing their growth behavior.

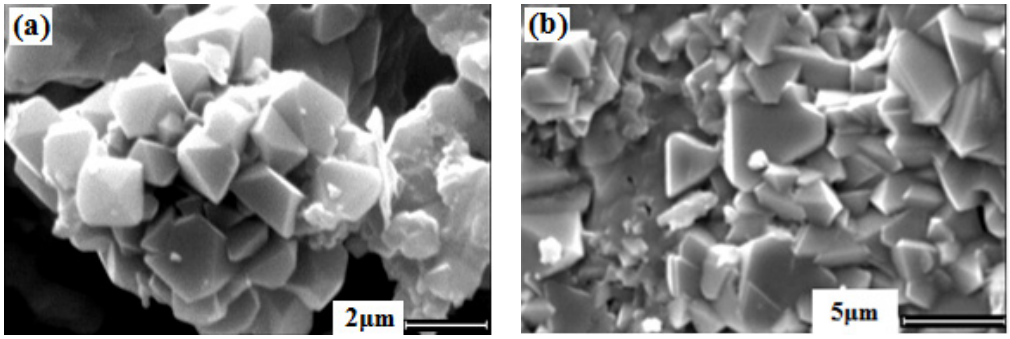

Figure 5. SEM micrographs of (**a**) spalled oxides and (**b**) oxidized sample after 50 h cyclic oxidation test at 1100 °C.

The surface morphology of the investigated alloy following 50 h and 100 h of cyclic oxidation at 1100 °C is depicted in Figure 6. After 50 h of exposure to the cyclic oxidation test, the oxides exhibit a pyramidal morphology, as illustrated in Figure 6a. However, with an increase in oxidation time, as shown in Figure 6b, the distinctive geometric shape of the oxides diminishes. Instead, the pyramidal oxides appear to merge, giving rise to a new form. Furthermore, the intersections between the edge planes of each pyramid become flattened, making it difficult to discern clear boundaries between the components of the oxide clusters. This transformation suggests that the pyramidal morphology of the oxides transitions into a nodular shape over time, driven by the reduction of the oxide's surface energy through the diffusion and movement of its constituent atoms.

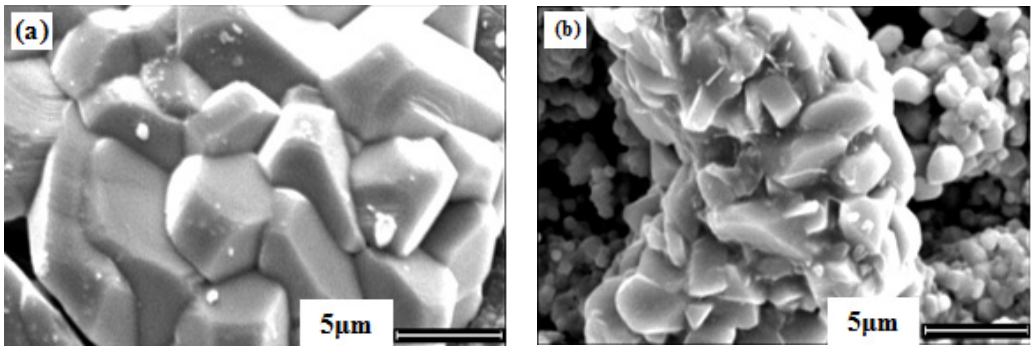

Figure 6. SEM images illustrating the surface morphology of the MA 754 samples after (**a**) 50 h and (**b**) 100 h exposure to cyclic oxidation at 1100 °C.

In order to gain further insights into the nature and composition of pyramidal-type oxides, EDS point analysis was employed. The results of this analysis conducted at points 1 and 2, as depicted in Figure 7a, are presented in Figure 7b,c. These point analyses were performed on the oxidized sample of MA 754 following a 100 h cyclic oxidation test at 1100 °C. The results reveal the presence of Ni, Cr, and O elements within the oxide pyramids. Considering the XRD pattern (Figure 2), which indicates the existence of NiO, $NiCr_2O_4$ and Al_2O_3 phases, it can be inferred that the pyramidal oxides are associated with the NiO and $NiCr_2O_4$ phases. Previous studies have reported a similar morphology for NiO and spinel oxides [26,29–32].

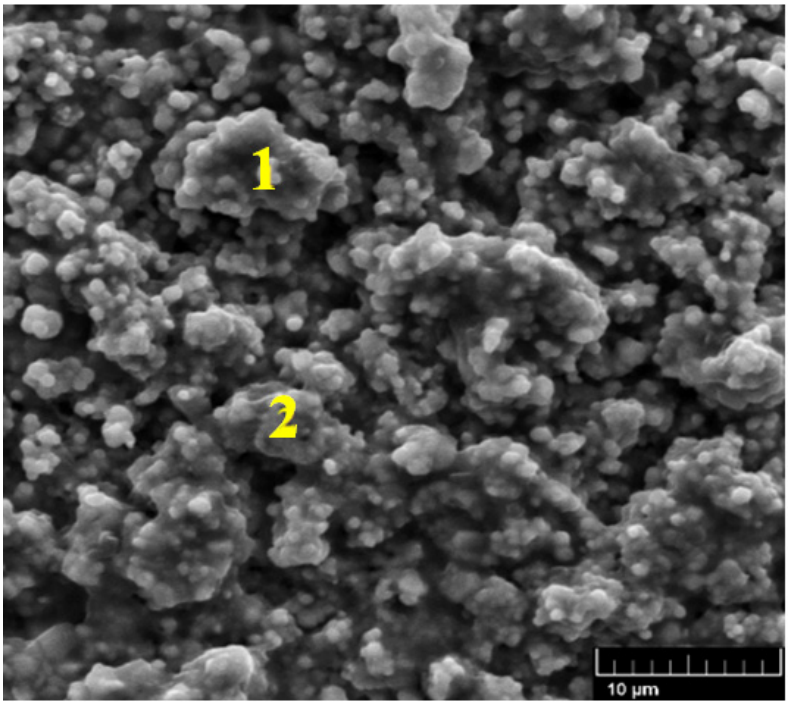
1
2
10 µm

(**a**)

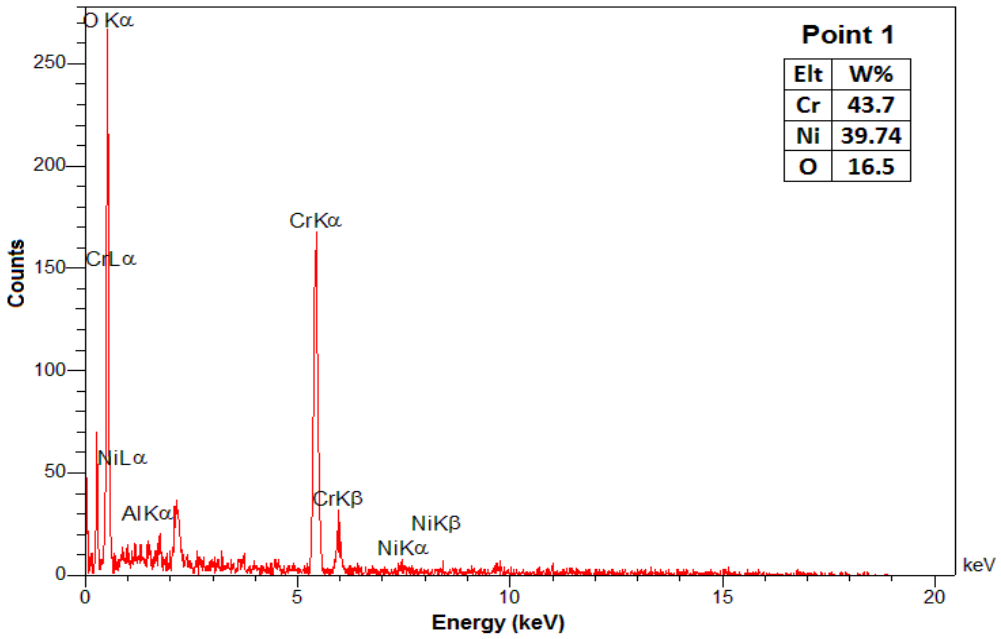
Point 1
Elt W%
Cr 43.7
Ni 39.74
O 16.5
O Kα
CrKα
CrLα
NiLα
AlKα
CrKβ
NiKβ
NiKα
Counts
Energy (keV)
keV
0
50
100
150
200
250
0
5
10
15
20

(**b**)

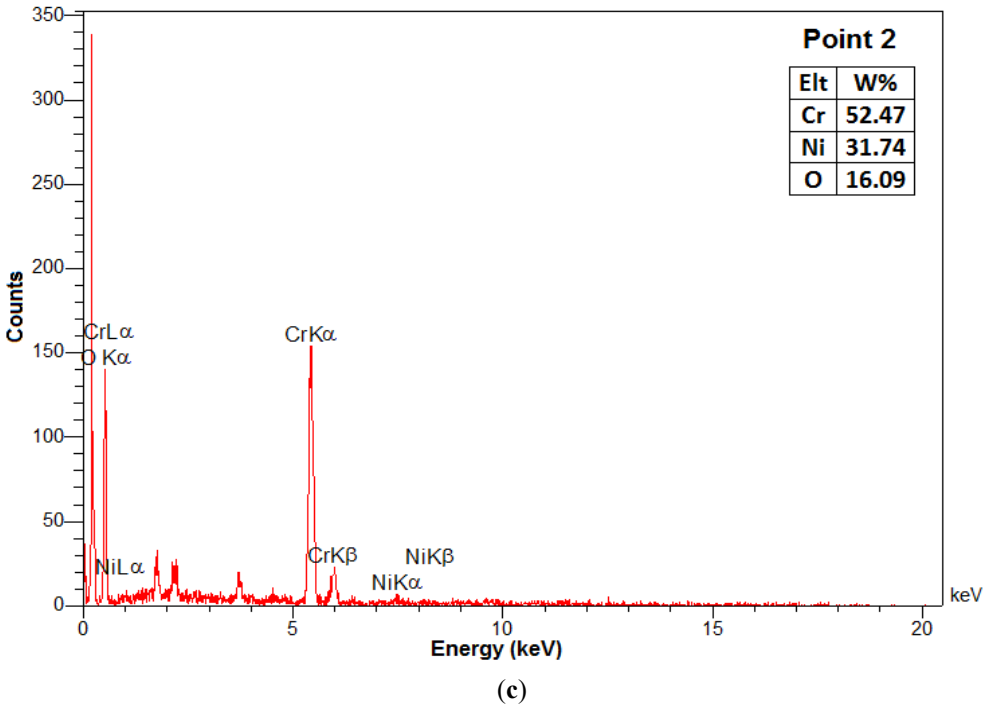

(**c**)

Figure 7. The EDS point analysis of the MA 754 sample after 100 h cyclic oxidation at 1100 °C (**a**), the EDS analysis of point 1 (**b**), The EDS analysis of point 2 (**c**).

3.4. Microstructure of Superalloy

Figure 8 shows the etched microstructure of the alloy surface before the oxidation test. This image clearly displays the numerous twins of the MA 754 that arise from the fabrication process.

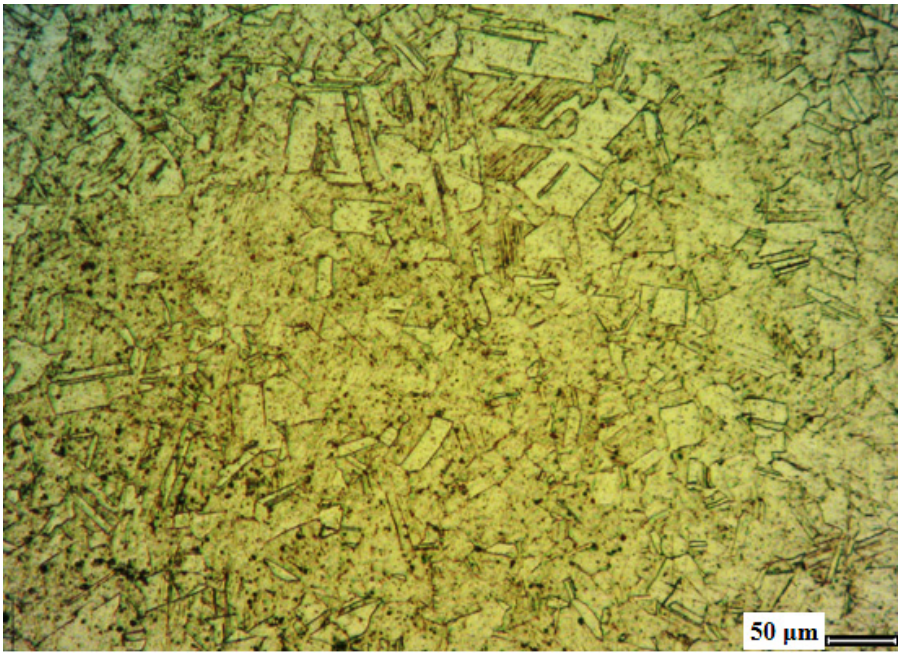

Figure 8. Microstructure of alloy surface before oxidation test, twins are visible in the surface of the superalloy.

The non-etched microstructure of the alloy surface prior to the oxidation study is presented in Figure 9a, revealing the presence of several fine porosities. Microstructures at different depths beneath the oxide layer, obtained after the oxidation test, are shown in Figure 9b–d. By comparing these microstructures, the oxidation process of the MA 754 superalloy can be characterized. The oxidation can be divided into three distinct stages, as follows:

1. In the initial stage, the grain boundaries undergo degradation due to the attack from the surrounding atmosphere, as depicted in Figure 9b. This degradation leads to the formation of voids along all grain boundaries. The voids

exhibit a continuous pattern, revealing the hexagonal arrangement of the grain boundaries. Previous studies have demonstrated that materials tend to experience preferential oxidation along grain boundaries, owing to their higher free energy compared to the grain regions. This preference facilitates faster intergranular transport of the reacting species [25,33,34]. Consequently, the degradation mechanisms of superalloys commence at the grain boundaries.

2. The second stage of the oxidation process ensues after the formation of voids along all grain boundaries. In this stage, high-energy regions within each grain, such as defects, twins, and porosities, are subject to degradation by the surrounding atmosphere. The presence of distinct voids within the grains, as shown on the left side of Figure 9c, indicates the occurrence of this step.
3. In the final stage, oxidation progresses in the remaining areas of the grains. Figure 9d illustrates the last step of oxidation, wherein more regions of the grains undergo degradation due to high-temperature oxidation. This process continues until the voids cover the entire surface of the sample.

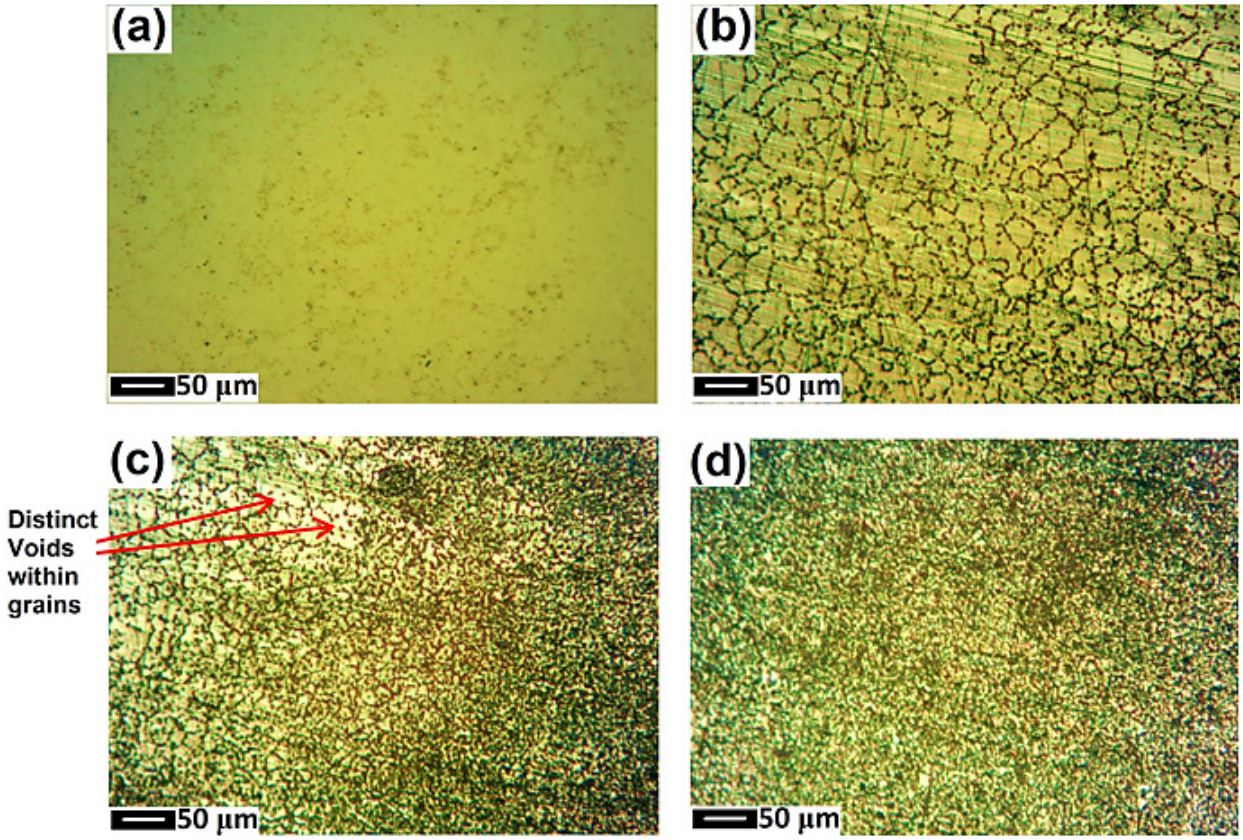

Figure 9. Microstructures of (**a**) alloy surface before oxidation test, (**b**–**d**) different depth under surface of the alloy beneath oxide layer at the end of cyclic oxidation test at 1100 °C.

4. Conclusions

The oxidation behavior of hot extruded MA 754 superalloy was investigated under cyclic conditions at 1100 °C. Our findings demonstrate that the oxidation kinetics of MA 754 exhibit a fluctuated oxidation behavior, indicating a non-steady oxidation response of the alloy under these conditions. Throughout the oxidation process, there is an average net mass increase of approximately 0.032 mg/cm^2. Initially, oxidation occurs primarily at the grain boundaries, followed by the degradation of high-energy regions within the grains, such as defects, twins, and porosities, due to atmospheric exposure. Gradually, the entire surface of the alloy undergoes gentle oxidation. The oxidation products identified are mainly NiO and $NiCr_2O_4$. Al_2O_3 may also be present in small amounts, based on weak XRD and EDS evidence.

Interestingly, the absence of Cr_2O_3 in the oxidation products suggests that this oxide is ineffective in protecting the alloy surface at 1100 °C. This absence of Cr_2O_3 can be attributed to the evaporation of the protective chromium oxide at high temperatures, as well as the reaction between NiO and Cr_2O_3, resulting in the formation of a non-protective $NiCr_2O_4$ spinel. Examination of the oxide scale formed during cyclic oxidation at 1100 °C through SEM micrographs reveals its porous nature and the presence of numerous cracks, indicating susceptibility to oxide spallation. Furthermore, the micrographs illustrate that the surface oxides exhibit a pyramidal morphology during the intermediate stages of the oxidation test. However, towards the end of the oxidation test, the pyramidal oxides transition into a granular

morphology, thereby reducing the surface energy of the oxides. Our XRD and EDS analyses confirm that the pyramidal-type oxides are primarily composed of NiO and $NiCr_2O_4$ phases.

Acknowledgments

The authors would like to thank the Department of Materials Science and Engineering at Shiraz University for providing access to laboratory facilities and technical equipment used in this study. We also acknowledge the support of laboratory staff for their assistance with SEM, XRD, and and EDS analyses.

Author Contributions

Conceptualization, M.J.H. and A.M.; Methodology, A.M.; Software, A.M.; Validation, A.M., M.J.H.; Formal Analysis, A.M.; Investigation, A.M.; Resources, M.J.H.; Data Curation, A.M.; Writing—Original Draft Preparation, A.M.; Writing—Review & Editing, M.J.H.; Visualization, A.M.; Supervision, M.J.H.; Project Administration, M.J.H.; Funding Acquisition, M.J.H.

Ethics Statement

Not applicable.

Informed Consent Statement

Not applicable.

Data Availability Statement

The statement is required for all original articles which informs readers about the accessibility of research data linked to a paper and outlines the terms under which the data can be obtained.

Funding

This research received no external funding.

Declaration of Competing Interest

The authors declare that they have no known competing financial interests or personal relationships that could have appeared to influence the work reported in this paper.

References

1. Atkinson R, Hunghes A. *High Temperature Corrosion*; Rapp R, Ed.; NACE: Houston, TX, USA, 1983.
2. Khanna AS. High temperature oxidation. In *Handbook of Environmental Degradation of Materials*, 3rd ed.; Kutz M, Ed.; William Andrew Publishing: Norwich, UK, 2018; pp. 117–132.
3. Khanna AS. *Introduction to High Temperature Oxidation and Corrosion*, 1st ed.; ASM International: Materials Park, OH, USA, 2002; pp. 1–306.
4. Obigodi-Ndjeng G. High Temperature Oxidation and Electrochemical Investigations on Nickel-Base Alloys. Ph.D. thesis, Erlangen-Nuernberg University, Erlangen, Germany, 2011.
5. Zheng L, Zhang MC, Dong JX. Hot corrosion behavior of powder metallurgy rene95 nickel-based superalloy in molten NaCl–Na_2SO_4 salts. *Mater. Des.* **2011**, *32*, 1981–1989.
6. Tang CF, Pan F, Qu XH, Duan BH, He XB. Nickel base superalloy GH4049 prepared by powder metallurgy. *J. Alloys Compd.* **2009**, *474*, 201–205.
7. Sidhu TS, Prakash S, Agrawal RD. Study of molten salt corrosion of superni-75 using termogravimetric technique. *J. Nav. Archit. Mar. Eng* **2008**, *3*, 77–82.
8. Kumar S, Mugal D, Singh S, Prakash S. Cyclic oxidation behavior of bare and Cr_3C_2–25 (NiCr) coated superalloy at elevated temperature. *Adv. Mater. Lett.* **2013**, *4*, 754–761.
9. Meethan G. High temperature materials in gas turbine engines. *Mater. Des.* **1998**, *9*, 213–219.
10. Donachie M, Donachie SJ. *Superalloys: A Technical Guide*, 2nd ed.; ASM International: Northeast, OH, USA, 2002.
11. Suryanarayana C, Ivanov E, Boldyrev V. The science and technology of mechanical alloying. *Mater. Sci. Eng.* **2001**, *304*, 151–158.
12. Suryanarayana C. Mechanical alloying and milling. *Prog. Mater. Sci.* **2001**, *46*, 1–184.

13. Khanna AS, Jha SK. Degradation of materials under hot corrosion conditions. *Trans. Indian Inst. Met.* **1998**, *51,* 279–290.
14. Grundy E, Patton WH. Properties and applications of hot formed ODS alloys. In *High Temperature Alloys*; Marriott J, Merz M, Nihoul J, Ward I, Eds.; Springer: New York, NY, USA, 1987; pp. 327–335.
15. Condé GFG, Erdös E, Rahmel A. Mechanisms of hot corrosion. In *High Temperature Alloys for Gas Turbines*; Brunetaud R, Coutsouradis D, Gibbons T, Lindblom Y, Meadowcroft D, Stickler R, Eds.; Springer: New York, NY, USA, 1982; pp. 99–148.
16. deBarbadillo JJ, Fcscher JJ. Dispersion-strengthened nickel-base and iron-base alloys in properties and selection: Nonferrous alloys and special-purpose materials. In *Oxidation of Metals, Metals Handbook*; ASM International: Northeast, OH, USA, 1990; pp. 943–949.
17. Quadakkers WJ. Oxidation of ODS alloys. *J. Phys. IV Fr.* **1993**, *3*, 177–186.
18. Mutoh Y, Hiraga K, Tanabe T. Corrosion behavior of Ni-base superalloys at 1373 K in simulated HTGR impure helium gas environment. *J. Nucl. Mater.* **1993**, *207*, 212–220.
19. Natesan K, Liu Y. Erosion-corrosion of materials at elevated temperatures/ *Mater. Sci. Eng* **1989**, *120*, 571–580.
20. Caplan D, Cohen M. The volatilization of chromium oxide. *J. Electrochem. Soc.* **1961**, *108*, 438–442.
21. Graham HC, Davis HH. Oxidation/ vaporization kinetics of Cr_2O_3. *J. Am. Ceram. Soc.* **1971**, *54*, 89–93.
22. Stearns CA, Kohl FG, Fryburg GC. Oxidative vaporization kinetics of Cr_2O_3 in oxygen from 1000 to 1300 °C. *Electrochem. Soc. Solid-State Sci. Technol.* **1974**, *121*, 945–951.
23. Asteman H, Svensson J, Johansson L. Norell M, Indication of chromium oxide hydroxide evaporation during oxidation of 304l at 873 K it the presence of 10% water vapor. *Oxid. Met.* **1999**, *52*, 95–111.
24. Opila E. Volatility of Common Protective Oxides in Water Vapor: Current Understanding and Unanswered Questions. *Mater. Sci. Forum.* **2004**, *461*, 765–774.
25. Pollock TM, Tin S. Nickel-based superalloys for advanced turbine engines. *J. Propuls. Power* **2006**, *22*, 361–374.
26. Young DJ. *High Temperature Oxidation and Corrosion of Metals*, 1st ed.; Elsevier: Amsterdam, The Netherlands, 2008.
27. Birks N, Meier GH, Pettit FS. *Introduction to the High Temperature Oxidation of Metals*, 2nd ed.; Cambridge university press: New York, NY, USA, 2006.
28. Hindam H, Whittle DP. Microstructure, adhesion and growth kinetics of protective scales on metals and alloys. *Oxid. Met.* **1982**, 18, 245–284.
29. Tang F, Ajdelsztajn L, Schoenung JM. Influence of cryomilling on the morphology and composition of the oxide scales formed on HVOF CoNiCrAlY coatings. *Oxid. Met* **2004**, *661*, 219–238.
30. Raynaud GM, Rap RA. In situ observation of whiskers, pyramids and pits during the high-temperature oxidation of metals. *Oxid. Met.* **1983**, *21*, 89–102.
31. Tawancy H. High-temperature oxidation behavior of a wrought Ni-Cr-W-Mn-Si-La alloy. *Oxid. Met.* **1996**, *45*, 323–348.
32. Jang CH, Kim D, Kim D, Sah I, Ryu WS, Yoo YS. Oxidation behaviors of wrought nickel-based superalloys in various high temperature environments. *Trans. Nonferrous Met. China* **2011**, *21*, 1524–1531.
33. Elzey DM, Arzt E. Oxide dispersion strengthened superalloys: The role of grain structure and dispersion during high temperature low cycle fatigue. *Metall. Soc.* **1988**, 595–604
34. Cao JD, Zhang JS, Chen RF, Ye YX, Hua YQ. High temperature oxidation behavior of Ni-based superalloy GH202. *Mater. Charact.* **2016**, *18*, 122–128.